Check for updates

Received: 12 April 2023 | Revised: 10 October 2023 | Accepted: 12 October 2023

DOI: 10.1002/fuce.202300057

Fuel Cells
From Fundamentals to Systems

RESEARCH ARTICLE

Microstructural changes in nickel-ceria fuel electrodes at elevated temperature

Yanting Liu[1] | **Florian Wankmüller**[2] | **Tibor Peter Lehnert**[2] | **Martin Juckel**[3] | **Norbert H. Menzler**[3] | **André Weber**[1]

[1]Institute for Applied Materials (IAM-ET), Karlsruhe Institute of Technology (KIT), Karlsruhe, Germany

[2]Laboratory for Electron Microscopy, Karlsruhe Institute of Technology, Karlsruhe, Germany

[3]Institute of Energy and Climate Research (IEK), IEK-1: Materials Synthesis and Processing, Forschungszentrum Jülich GmbH, Jülich, Germany

Correspondence
Yanting Liu, Institute for Applied Materials (IAM-ET), Karlsruhe Institute of Technology (KIT), Adenauerring 20b, 76131 Karlsruhe, Germany.
Email: yanting.liu@kit.edu

Paper presented at the 15th European SOFC & SOE Forum 2022, held 5-8 July in 2022 in Lucerne, Switzerland. Organized by the European Fuel Cell Forum www.efcf.com

Funding information
Federal Ministry of Education and Research, Grant/Award Number: BMBF 03SF0622E

Abstract

Durability testing of low temperature solid oxide cells is challenging as degradation phenomena related to microstructural changes like nickel-agglomeration are slow. In the present study, a nickel/gadolinia doped ceria (GDC) fuel electrode with a porous GDC-interlayer towards the zirconia electrolyte was investigated. The electrode, designed for operating temperatures of 600°C, was tested at an elevated temperature of 900°C for up to 1100 h to accelerate aging. Contrary to every expectation, the electrodes showed continuous improvement in electrochemical performance. Impedance spectroscopy, the distribution of relaxation times analysis, scanning electron microscope and transmission electron microscope were applied to correlate electrochemical and microstructural changes. Structural analysis showed a significant Ni agglomeration accompanied by a decrease in triple phase boundary density. Furthermore, a minor particle growth in the GDC-phase decreased the volume-specific double phase boundary GDC/pore. Considering these microstructural changes, the decrease in active reaction sites should have increased the polarization resistance, but a decrease of about 32% was observed. The discrepancy between polarization resistance improvement and microstructural degradation might be attributed to an activation of the GDC-surfaces in the electrode and the porous GDC-interlayer.

KEYWORDS
durability, impedance spectroscopy, microstructure, SOC, surface activation, SEM, TEM

1 | INTRODUCTION

Several studies on Ni/yttria-stabilized zirconia (Ni/YSZ), which is a state-of-the-art electrode for high-temperature fuel cells, have related performance degradation to microstructural changes [1–3]. Main degradation phenomena in such electrode are Ni agglomeration and coarsening [4, 5], sulphur poisoning [6, 7] and carbon

List of Symbols: A, contact area density between 2 phases/m^{-1}; d, average particle size d_{50} / m; f, frequency / Hz; GDC, gadolinium doped ceria; l_{TPB}, triple phase boundary density / m^{-2}; Ni, nickel; pol, polarization; Pore, pore; R_{pol}, polarization resistance / Ω m^2; R_{react}, electrochemical reaction resistance / Ω m^3; T, temperature / K; t, time/s; TPB, triple phase boundary; ε, volume fraction; τ, effective tortuosity.

This is an open access article under the terms of the Creative Commons Attribution-NonCommercial License, which permits use, distribution and reproduction in any medium, provided the original work is properly cited and is not used for commercial purposes.
© 2023 The Authors. Fuel Cells published by Wiley-VCH GmbH.

deposition [8, 9]. The grain growth of nickel is generally considered to be the most prominent factor [10, 11]. Various studies have discussed its dependence on operating parameters. Thydén revealed that increase in steam concentration could accelerate the nickel coarsening [12]. It was also reported that the Ni agglomeration is favoured when the temperature increases [13, 14]. Thus, understanding solid oxide cell (SOC) degradation mechanisms related to microstructural changes is essential to predict and enhance lifetime of solid oxide fuel cells (SOFCs) [15].

A transmission line model (TLM) can relate polarization resistance and structural parameters quantitatively [16]. Till this level, the aging empirical function is deconvoluted to the relationship between time and structural parameters, such as particle size distribution (PSD), tortuosity, specific active area and triple phase or double phase boundary (TPB, DPB) density. To predict the calendar life of SOFC within a short testing duration, the degradation in microstructure has to be accelerated by a suitable aggravated stressor. The lifetime prediction is realized by extrapolation to nominal stressor after obtaining degradation-time distribution with varying the aggravated stressors [17–20].

The relationship between stressors and degradation mechanism based on different electrochemical or physical theories is very complex. Since the number of tests is also strictly restricted, the statistic derived empirical model is a good substitution. The distributive character of the measured times to failure according to huge deviation between measured and estimated lifetime was claimed in [21]. In a full cell, several degradation mechanisms together influence cell performance with varying weights along different temperatures, gas compositions, loads and time. As consequence, the statistic empirical model is only valid inside short time where one aging mechanism is dominant. It is thus necessary to deconvolute the different aging mechanism contributions along time [22]. In previous work of our group, the resistance of a full cell was already deconvoluted to two major processes (gas diffusion and charge transfer related) in both electrodes and the ohmic resistance dominated by the electrolyte [22]. In case of physicochemical meaningful equivalent circuit models as the Gerischer element describing the oxygen reduction in mixed ionic and electronic conductor (MIEC) -cathodes, the aging can be related to changes in microstructural and material parameters [23]. The investigations revealed different operating parameter dependencies of the different aging processes. Aging of the fuel electrode was thermally activated, the aging of the air electrode increased with decreasing temperature. To avoid such contrary dependencies and simplify the analysis process, symmetrical cells are a good choice to study the durability of a single electrode.

Several investigations have been carried out on structural evolution of commonly used Ni/ceria in SOFC anodes. The main aging phenomenon is attributed to Ni coarsening, agglomeration and depletion [15, 24], similar to Ni/zirconia cermets. The zirconia matrix is commonly stable whereas microstructural changes in the gadolinia doped ceria (GDC) were observed in Ni/GDC mixtures [4, 15, 25]. An extra witnessed phenomenon in Ni/GDC is GDC coating of Ni-surfaces. The coating prohibits Ni coarsening, but also blocks mass transport and decreases TPB density and might even affect Ni percolation. The GDC coating of Ni-surface is a nominal aging mechanism observed after ~15 000 h [4, 15]. With particle growth, the Ni-Ni and Ni-GDC contacts get lost gradually, thus lead to decrease in TPB density and increase in electronic resistance. Ni depletion leads to a decrease of the active reaction sites within the active part of the electrode layer. Furthermore, Ni-loss might also result in a dramatic increase in ohmic resistance. The quantitative investigation on Ni particle size evolution reveals temperature and humidity strengthened growth. The growth is faster in initial 200 h and later prohibited by coating of GDC after 15,000 h, the quantitative particle size evolution under different condition is stated in [4].

Ouyang et al. reported dynamic Ni migration at active TPB in patterned Ni/YSZ electrode under SOFC mode [26]. The nano-Ni particles separated from the main Ni network remained active. Similar Ni spreading and splitting was observed in patterned Ni/GDC electrodes by the same group [27]. However, after initial wetting of Ni on GDC particle, the movements of both Ni and GDC in the range of tens of micrometers were seen. GDC nano-particles were also found in Ni phase.

In this work, symmetrical cells with Ni/GDC electrodes, designed for operation at 600°C, were tested at elevated temperature and humidity to accelerate abovementioned microstructural changes and related degradation. *Post mortem* analyses revealed the expected microstructural changes, decreasing triple and double phase boundary densities. In contrast, a continuous improvement in electrochemical performance was witnessed instead of the expected aging. The mechanism competing with other degradation mechanisms might be the activation of GDC-surfaces due to Ni deposition.

2 | EXPERIMENTAL

In this paper electrolyte-supported symmetrical cells (ESC) with Ni/GDC-electrodes (1 cm^2) manufactured at Forschungszentrum Jülich GmbH were investigated. The tested cells consist of a thick 8 mol.% YSZ electrolyte (200 μm) (Kerafol GmbH, Eschenbach, Germany), two

16156854, 2023, 6, Downloaded from https://onlinelibrary.wiley.com/doi/10.1002/fuce.202300057 by Forschungszentrum Jülich GmbH Research Center, Wiley Online Library on [05/01/2024]. See the Terms and Conditions (https://onlinelibrary.wiley.com/terms-and-conditions) on Wiley Online Library for rules of use; OA articles are governed by the applicable Creative Commons License

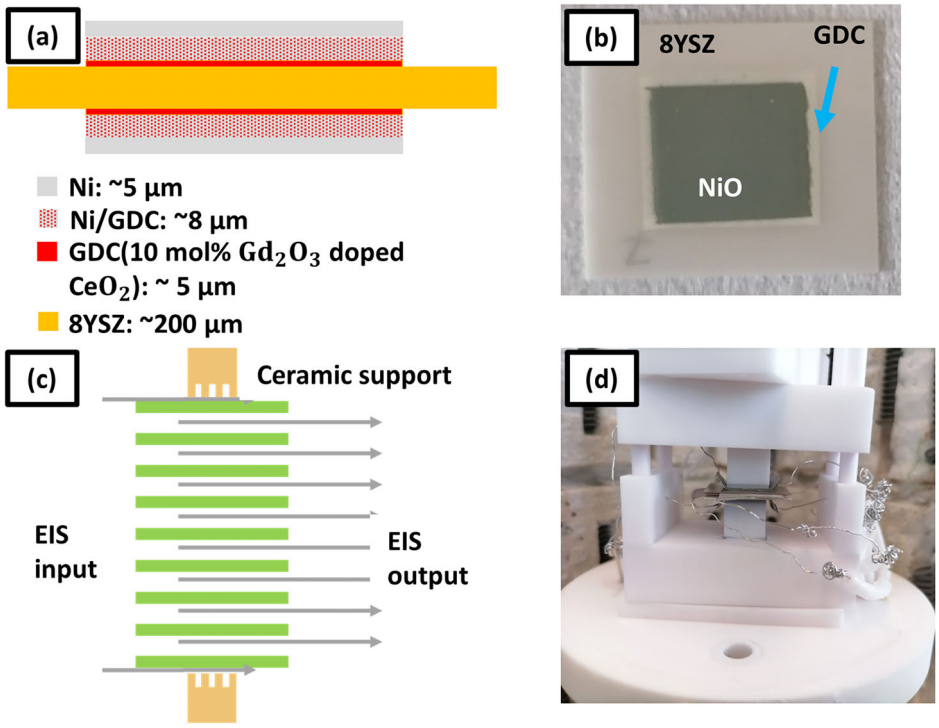

FIGURE 1 Schematic of cell structure and setup for multi cell test with an active driven gas layer stack. (a) Schematic sketch of symmetrical cell with Ni/gadolinia doped ceria (GDC) fuel electrodes, GDC-interlayers and an 8YSZ electrolyte. (b) Image of top view of the unreduced cell. (c) Schematic illustration of the active driven gas layer stack. The capacity of this setup is seven inner cells sandwiched between two outer cells. The Ni meshes (grey arrows) are placed between the cells for voltage measurement and at the two outer sides for (ac and dc) current supply. (d) The real setup with four stacked cells in the test bench.

symmetrical porous GDC-interlayers (5 µm), two Ni/GDC anodes (8 µm) and two Ni current collector layers (4 µm) (Figure 1a-b). All layers were screen printed onto the 8YSZ-substrate and co-fired. For detailed production procedure, please refer to [28]. A scanning electron microscope (SEM) image (Figure 7a) shows the porous electrode structure after reduction.

Up to four cells were stacked in an open ceramic sample holder (Figure 1d) using an active driven gas layer concept. In this stack with a highly porous Ni-grid between two neighboring electrodes, the fuel consumed at one of these electrodes is produced at the other, resulting in a purely perpendicular gas transport avoiding any impact of flow rate and flow field geometry. Only the outer cells of this stack are contacted by a Ni-grid attached to a ceramic flow field and thus are not symmetrical considering the different gas transport properties at the electrodes (Figure 1c). Consequently, results from the outer cells cannot be used. The humidification was realized by burning a part of the hydrogen with oxygen in an upstream burner. A ceramic hood is placed over the whole setup, the internal gas composition is monitored by a lambda sensor. Other parts of the test bench are described in detail in [29].

The cells were heated up to 800°C in nitrogen and gradually reduced in hydrogen/nitrogen mixtures. After adjustment of gas composition to hydrogen (0.5 L min^{-1}) and oxygen (0.125 L min^{-1}) producing a hydrogen/steam-mixture of 1:1 in the upstream burner [29], the cells were characterized with electrochemical impedance spectroscopy (EIS) at 800, 650 and 600°C. At the end of this initial characterization, the furnace was heated up to achieve a cell temperature of 900°C. The cell performance evolution was recorded by means of continuous impedance measurements. All impedance measurements were performed at open-circuit voltage (OCV) conditions to ensure the electrochemical symmetry of both electrodes.

Three cells from the same batch were tested. Cell 1 was only reduced and not aged. Cell 2 was operated for 240 h. Cell 3 was operated for 1100 h. Reference measurements at 600°C with the same gas composition were carried out by cell 3.

During operation at 900°C, an unexpected long (700 h) decrease of the polarization resistance of the electrodes was observed in cell 3. This extraordinary long phase of electrode improvement was very different from the reported "wear-in" phases in the range of several hours to a few days [30] and cannot be neglected in a 1100 h test.

For post-test analysis, the only reduced cell 1 and the operated cell 2 were cracked into pieces and infiltrated, cut, polished for SEM (Zeiss CrossBeam XB 1540, Carl

16156854, 2023, 6, Downloaded from https://onlinelibrary.wiley.com/doi/10.1002/fuce.202300057 by Forschungszentrum Jülich GmbH Research Center, Wiley Online Library on [05/01/2024]. See the Terms and Conditions (https://onlinelibrary.wiley.com/terms-and-conditions) on Wiley Online Library for rules of use; OA articles are governed by the applicable Creative Commons License

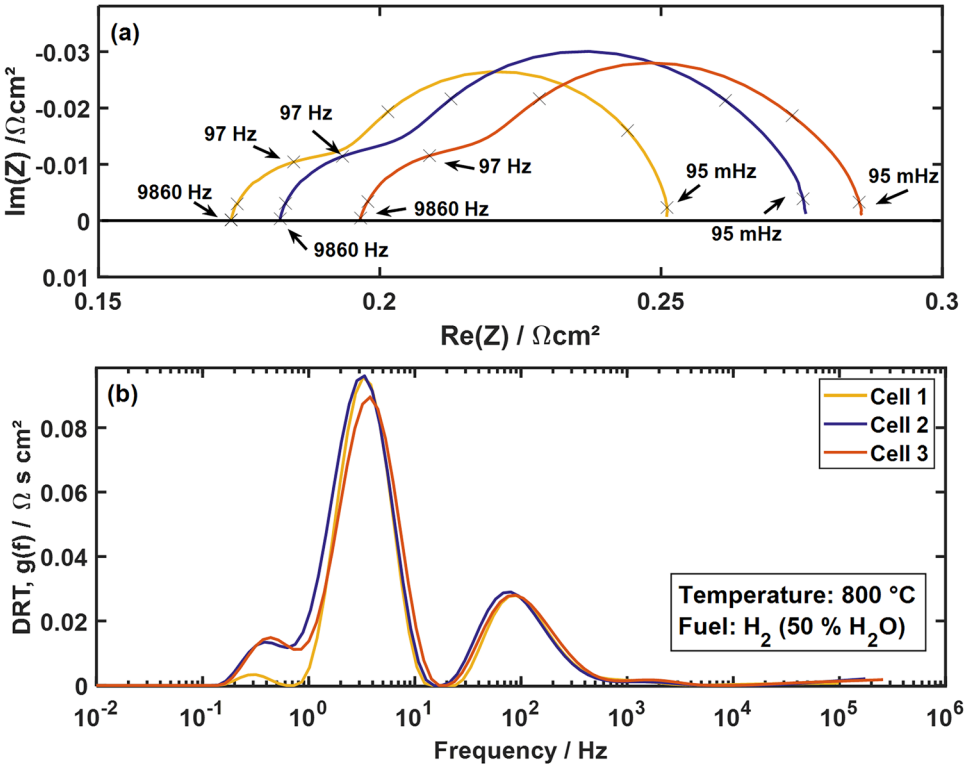

FIGURE 2 (a) Impedance spectra of three tested cells at 800°C. The values are halved for single electrode evaluation. (b) Corresponding DRTs.

Zeiss AG, Oberkochen, Germany) and energy dispersive X-Ray analysis (EDS) (XFlash Detector 5030, Bruker AXS, Karlsruhe, Germany). Reconstruction work via focused-ion-beam (FIB)-SEM Thermo ScientificTM Helios G4FX DualBeamTM (Thermo Fisher Scientific, Waltham, Massachusetts, USA) was carried out afterwards. The FIB-SEM procedure and subsequent data analysis are described in [31, 32]. Cell 3 was also analyzed by scanning transmission electron microscopy (STEM) including EDS (OSIRIS ChemiStem, Thermo Fisher Scientific, Massachusetts, USA) analysis. Details about sample preparation and analysis can be found in [33, 34].

3 | RESULTS AND DISCUSSION

3.1 | Time evolution of cell resistances

The 3 cells initially showed polarization resistances of 0.077, 0.093 and 0.089 Ω cm^2 per electrode (800°C, 50% H_2 + 50% H_2O). In Figure 2, the related impedance spectra and distribution of relaxation time (DRT) are displayed. The DRTs show differences in the small peak below 1 Hz and minor ones in the main peak at 3 Hz whereas a good agreement is observed for higher frequencies. Since they are related to electrochemical reactions and transport processes happening in the electrode, their correspondence suggests a good reproducibility in microstructure. A moderate reproducibility is also witnessed in the polarization resistance evolution of cell 2 and 3. Despite the rather identical initial values, cell 2 shows a slightly larger improvement during the first 250 h of operation (Figure 3) at 900°C. In conclusion, the cells showed an acceptable reproducibility in initial performance and the microstructural differences between the three cells after testing most probably have to be attributed to high temperature and humidity-related structural and material changes.

Figure 4 shows impedance spectra and related DRTs of cell 3 measured during 1100 h test at 900°C. Full quantitative presentation of resistance changes is given in Figure 3. The timespan between 500 and 535 h and around 820 h are an oxygen supply interruption and a reference measurement at 600°C, respectively. As to be expected, the ohmic resistance shows an increase, which is at least partially related to the intrinsic conductivity degradation of the zirconia electrolyte [35]. Regarding the electrode polarization, it is visible that a significant decrease in polarization resistance took place in the first 200 h. After that, the decrease slows down and reached a final value after about 650 h.

The observed improvement can only be attributed to complex structural and/or material changes within the

16156854, 2023, 6, Downloaded from https://onlinelibrary.wiley.com/doi/10.1002/fuce.202300057 by Forschungszentrum Jülich GmbH Research Center, Wiley Online Library on [05/01/2024]. See the Terms and Conditions (https://onlinelibrary.wiley.com/terms-and-conditions) on Wiley Online Library for rules of use; OA articles are governed by the applicable Creative Commons License

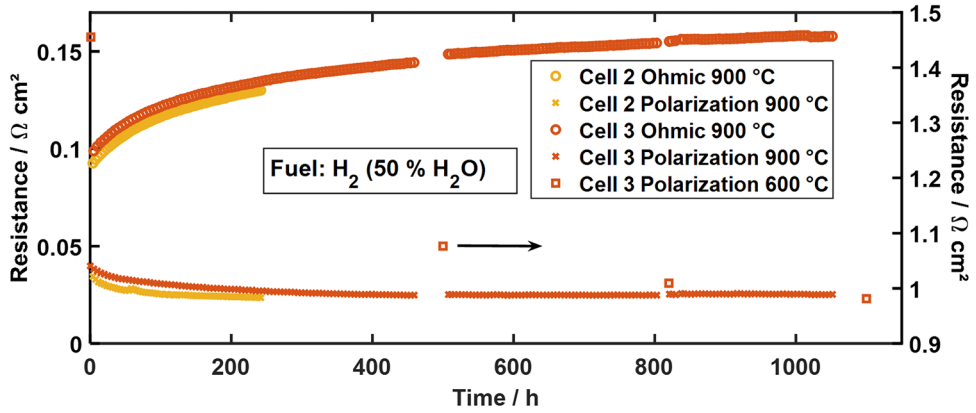

FIGURE 3 Time evolution of ohmic and polarization resistance measured at 900°C in a hydrogen/steam-mixture of 1:1 of cell 2 and 3 plotted to the left axis. Polarization resistance of reference measurement results of cell 3 at 600°C under same gas composition are plotted to the right axis. The values are halved for single electrode evaluation.

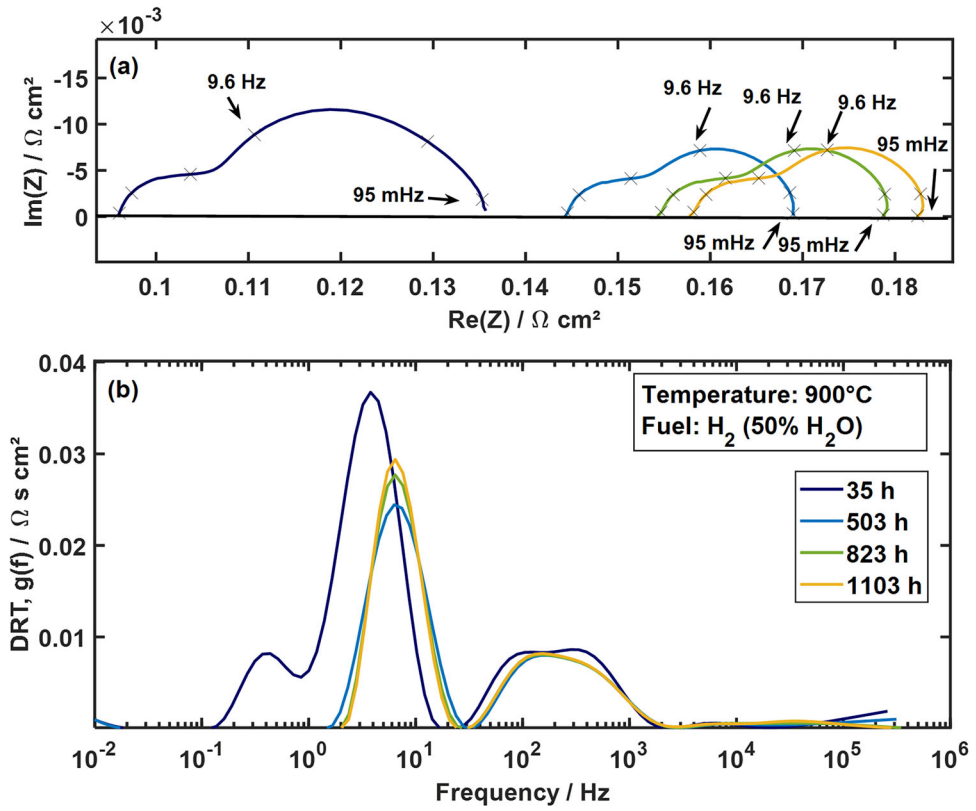

FIGURE 4 (a) Time evolution of impedance spectra of symmetrical Ni/gadolinia doped ceria (GDC) anode cell 3 under OCV at 900°C in a hydrogen/steam-mixture of 1:1. (b) Corresponding DRTs. The values are halved for single electrode evaluation.

electrode layer. From the DRTs, displayed in Figure 4b, it is clear that the improvement mainly happened to the peak between 1–30 Hz, which is related to gas diffusion and the charge transfer reaction overlapping in the DRT [36].

A decrease in R_{pol} was also witnessed during the initial operation phase of anode-supported cells exhibiting a Ni/YSZ cermet anode and substrate [30]. By means of DRT analysis it could be related to improved gas diffusion in the anode substrate. In the actual study, R_{pol} decreased to 60% of the original value within 650 h at 900°C (Figure 3). This improvement cannot be allocated to improved gas diffusion resistance as it is also visible in the reference measurements carried out at 600°C (Figure 5). R_{pol} decreases by 0.47 Ω cm^2 after 1,100 h of operation at 900°C (Figure 3). This difference is several times larger than the overall polarization loss at 900°C and thus cannot be attributed to a change in the approximately temperature independent gas diffusion resistance.

16156854, 2023, 6, Downloaded from https://onlinelibrary.wiley.com/doi/10.1002/fuce.202300057 by Forschungszentrum Jülich GmbH Research Center, Wiley Online Library on [05/01/2024]. See the Terms and Conditions (https://onlinelibrary.wiley.com/terms-and-conditions) on Wiley Online Library for rules of use; OA articles are governed by the applicable Creative Commons License

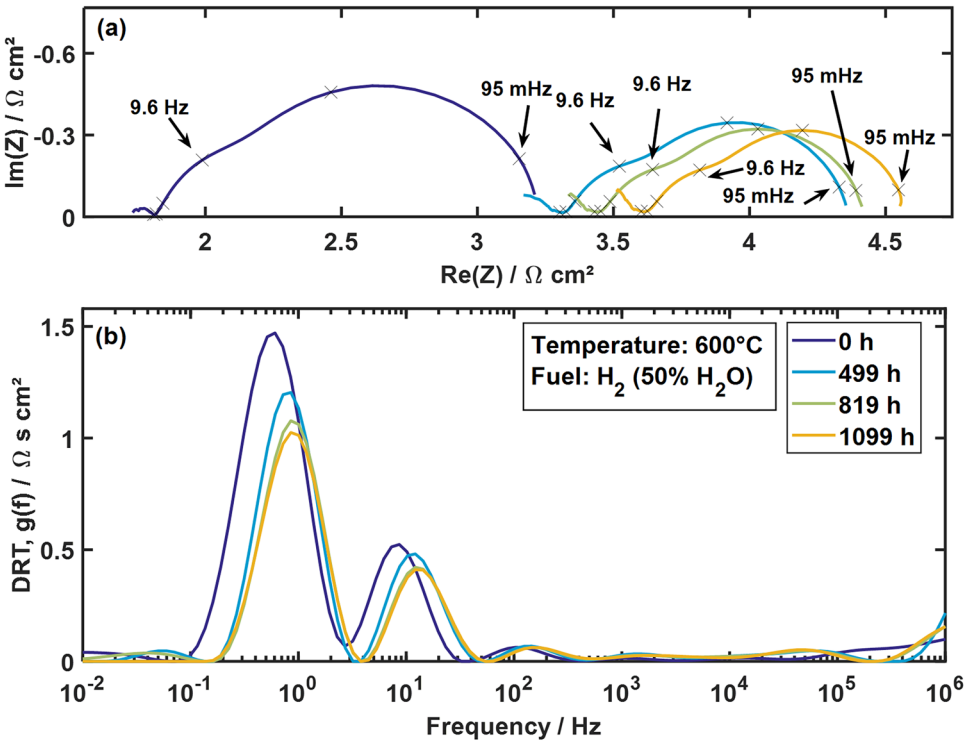

FIGURE 5 (a) Time evolution of reference impedance spectra of symmetrical Ni/gadolinia doped ceria (GDC) anode cell 3 under OCV at 600°C in a hydrogen/steam-mixture of 1:1. (b) Corresponding DRTs. The values are halved for single electrode evaluation.

Based on the relationship between material, structure and performance presented in [16], the lowering of this peak and its movement towards higher frequencies has to be attributed to a decrease of the electrochemical reaction resistance R_{react}, corresponding to an increase in electrocatalytic activity and/or density of active reaction sites. In case of the mixed ionic electronic conducting GDC-backbone, an increase in active reaction sites is not limited to the continuous Ni-matrix but also TPBs of single Ni-particles on the GDC-surface as well as the GDC-surface itself. To figure out the background of the huge change in R_{pol}, the samples were investigated by means of electron microscopy in post-test analysis.

3.2 | Post-test analysis

One possible explanation for a performance increase would be Ni transport into the porous GDC-interlayer located underneath the Ni/GDC anode layer. Considering temperature and humidity, surface diffusion is highly possible. Besides, Ni spreading and splitting phenomena were reported on both Ni/GDC and Ni/YSZ electrodes [26, 27]. As a result, additional active reaction sites could be formed by Ni deposited on GDC-surfaces inside the porous GDC-interlayer.

The distribution of Ce and Ni analyzed by means of EDS is shown in Figure 6, displaying from left to right the SEM image, the overall EDS-mapping and the distribution of Ce and Ni for cell 1 (Figure 6a1–a4) and 2 (Figure 6b1–b4), respectively. The SEM images acquired by an SE detector do not reveal any clear contrast between Ni and GDC-phase. It is obvious that in cell 1, both in GDC-interlayer and Ni/GDC anode layer, particles are smaller in average size compared to those in the operated cell 2. The contrast in the YSZ substrate in cell 1 is due to a local depth difference resulting from the sample preparation by cracking. The EDS mappings reveal an interdiffusion of Gd and Ce into the YSZ-substrate. In the Ni distribution mapping, no Ni could be detected within the porous GDC-interlayer. Since EDS mapping is only sensitive to mass fractions exceeding 1% and a large area fraction of the cross section is intergranular, a deposition of Ni on the GDC-surfaces in the porous GDC-interlayer cannot be excluded. Considering that nanoscale electrocatalysts can exhibit a rather high activity, the electrode improvement due to Ni-transport into the GDC-interlayer is feasible despite no Ni was observed by EDS.

FIB-SEM reconstructions of the 2 cells were carried out to quantify microstructural parameters of the Ni/GDC anode layer. Cross-sections of the 2 cells are presented in Figure 7. For cell 1 the reconstruction was limited to

16156854, 2023, 6, Downloaded from https://onlinelibrary.wiley.com/doi/10.1002/fuce.202300057 by Forschungszentrum Jülich GmbH Research Center, Wiley Online Library on [05/01/2024]. See the Terms and Conditions (https://onlinelibrary.wiley.com/terms-and-conditions) on Wiley Online Library for rules of use; OA articles are governed by the applicable Creative Commons License

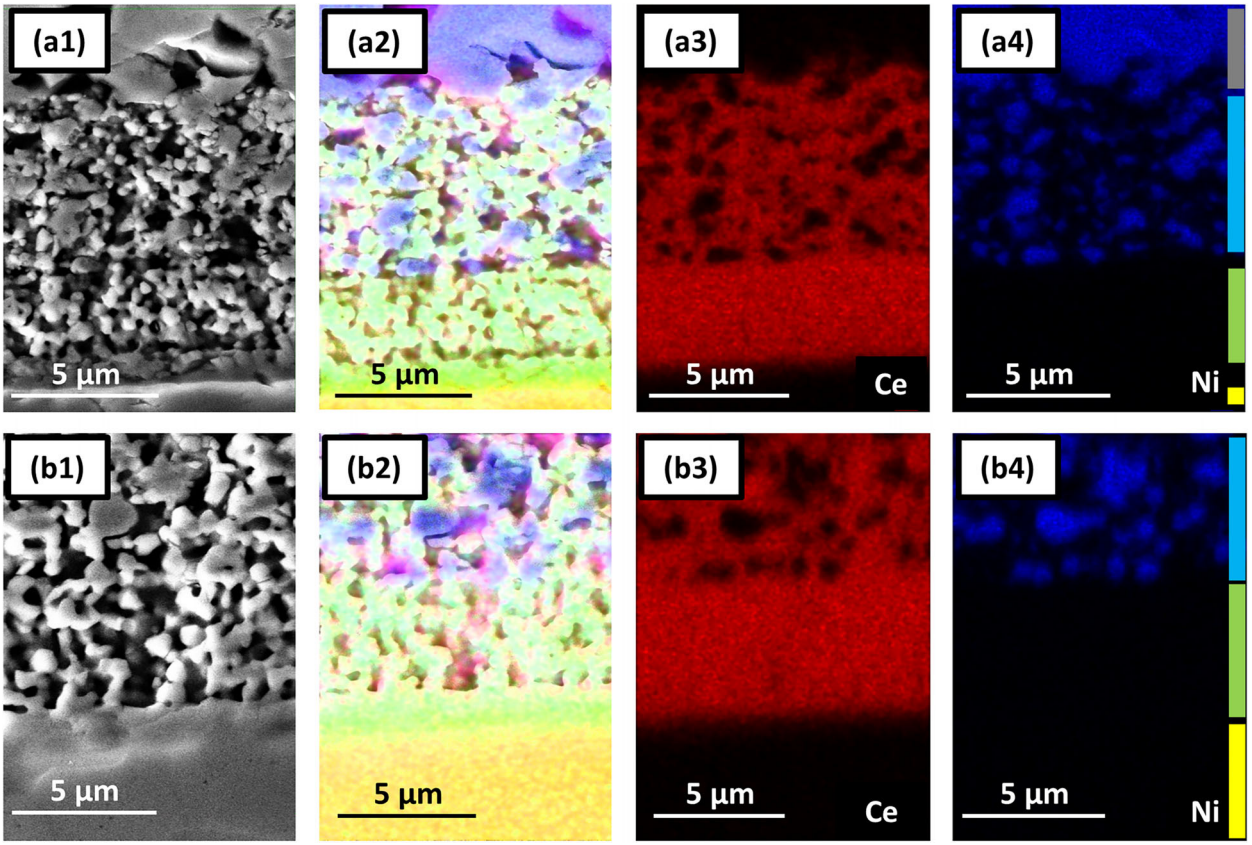

FIGURE 6 Scanning electron microscope (SEM) and EDS mapping of (a1-a4) reference cell 1 and (b1-b4) operated cell 2. From left to right are (1) SE images (voltage 1.3 kV), (2) overlapped EDS mapping of elements Ni (blue), Ce (red), Gd (green), Y(orange) and Zr (yellow), and separate (3) Ce and (4) Ni mapping. In (a4) and (b4), the YSZ layers are marked in yellow, gadolinia doped ceria (GDC) layers in green, Ni/GDC layers in blue and Ni contact layer in grey.

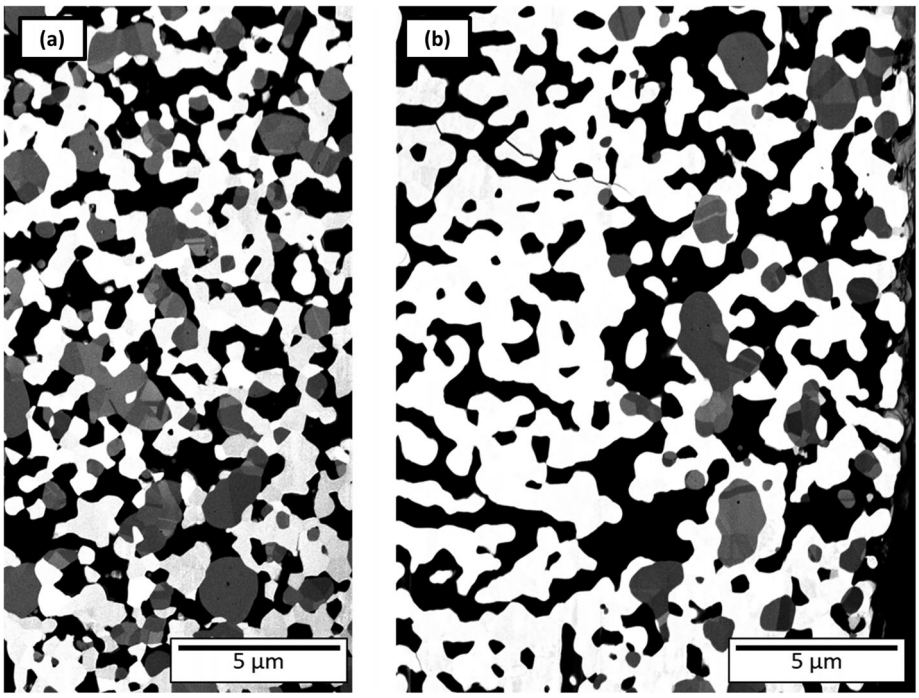

FIGURE 7 Backscatter electron (BSE) images (voltage 3 kV) presenting FIB cross sections of (a) Ni/gadolinia doped ceria (GDC) anode of cell 1, (b) GDC-interlayer and Ni/GDC anode of cell 2. In the images, black corresponds to pores, white to GDC and grey to Ni.

16156854, 2023, 6, Downloaded from https://onlinelibrary.wiley.com/doi/10.1002/fuce.202300057 by Forschungszentrum Jülich GmbH Research Center, Wiley Online Library on [05/01/2024]. See the Terms and Conditions (https://onlinelibrary.wiley.com/terms-and-conditions) on Wiley Online Library for rules of use; OA articles are governed by the applicable Creative Commons License

TABLE 1 Microstructural parameters of cell 1 and 2 derived via FIB-SEM.

Parameter	Cell 1	Cell 2
Testing conditions	Reduced	Operated 240 h
reconstructed volume/ μm^3	1686	1542
ε_{pore} / %	36	38
ε_{GDC} / %	44	42
ε_{Ni} / %	20	20
l_{TPB} / μm^{-2}	3.57	1.94
$A_{Ni\text{-}Pore}$ / μm^{-1}	0.59	0.33
$A_{GDC\text{-}Pore}$ / μm^{-1}	1.95	1.77
$A_{GDC\text{-}Ni}$ / μm^{-1}	0.80	0.74
τ_{Pore} / –	2.47	2.12
τ_{GDC} / –	2.32	2.45
d_{pore} / µm	0.43	0.55
d_{GDC} / µm	0.50	0.56
d_{Ni} / µm	0.38	0.65

the Ni/GDC anode layer while Ni/GDC anode layer and GDC-interlayer were analyzed for cell 2. Compared to cell 2, the Ni/GDC layer of cell 1 has a finer structure with smaller average particle sizes for both Ni and GDC. This is quantified by the structural parameters from reconstruction, as presented in Table 1 (only Ni/GDC anode layer considered). The given tortuosities represent the effective transport parameter for electronic, ionic or gas phase transport [32]. Both cells exhibit a quite similar composition. The TPB density of cell 2 has decreased by 46% from 3.57 to 1.94 μm^{-2}, the DPB density $A_{GDC\text{-}Pore}$ by 9%. Both DPB and TPB density changes indicate degradation in electrode performance. The same holds for the tortuosity of the GDC-phase τ_{GDC}, predicting a decrease in GDC conductivity. The only microstructural parameters indicating possible improvement in R_{pol} are d_{Pore} and $\tau_{Pore.}$ However, the improvement in gas diffusion was already excluded above. Based on these results, an aging of the cell has to be expected, which was not observed in the electrochemical measurements.

Nevertheless, changes might have taken place on an nm-scale [26, 27] not resolvable in FIB-SEM reconstructions. Sciazko reported multiscale microstructural evolutions of Ni/GDC in SOFC mode [37]. They investigated an electrolyte-supported cell consisting of LSCF cathode, electrolyte, Ni/GDC anode and Ni top layer. After 100 h at 0.2 A cm^{-2} load and 40% H_2: 20% H_2O: 40% N_2 of gas supply at 800°C, the polarization resistance increased by 50%. In contrary to worsening performance, structural analysis revealed higher TPB and DPB densities. They attributed this controversy to electrode inhomogeneity after test. Significant GDC-migration and creation of nano-sized GDC-layers was found on Ni surfaces. The newly developed Ni/GDC DPB appeared closer to the current collector. On the other hand, a decrease in GDC portion, DPB- and TPB-density was witnessed close to the electrolyte in that paper.

In Figure 8, SEM-images of fractured cross sections of cell 1 and 2 are shown. The samples were prepared by just cracking the cells and thus show the uneven surfaces of the crack (Ni/Ni, Ni/GDC, GDC/GDC) as well as Ni and GDC particle surfaces (Ni/pore, GDC/pore). The Ni particle surface in cell 1 is rather smooth (Figure 8a). Some sub-µm sized Ni particles are witnessed. Figure 8b shows a fine substructure on the Ni surface of cell 2. The impact of such Ni surface roughness is unclear. From Figure 8, we have not seen any evidence of nano-GDC particle or nano-scale changes in GDC phase.

To analyze further structural changes, (scanning) TEM (STEM) analysis was performed with cell 3 previously aged for 1100 h at 900°C. Figure 9 displays the FIB-milled TEM sample in the SEM. The STEM-analysis considers GDC-interlayer (Window I), Ni/GDC anode layer (Window III) and the transition zone of both layers (Window II). The area in the three windows was thinned to about 100 nm in a Helios G4FX by FIB. STEM Imaging was performed using a high-angle annular dark-field detector (HAADF-STEM).

Figure 10 shows the results of window I. The HAADF image given in (Figure 10a) indicates the presence of

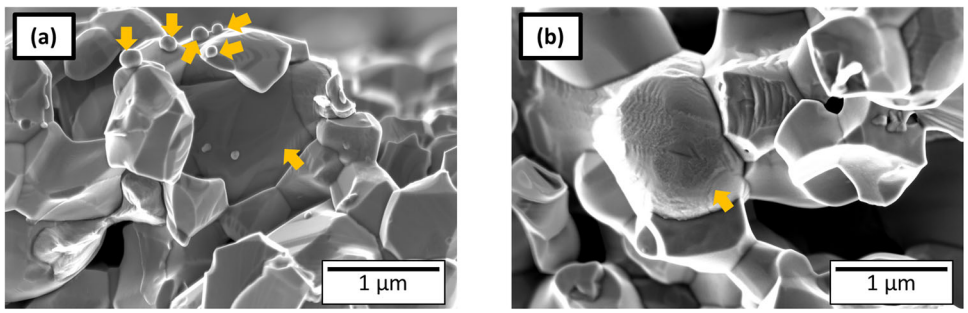

FIGURE 8 Scanning electron microscope (SEM) (3 kV) images presenting surface of (a) Ni particle in the reference cell 1 and (b) Ni particle of cell 2. The Ni particles are indicated with yellow arrows. Other particles in view are gadolinia doped ceria (GDC).

16156854, 2023, 6, Downloaded from https://onlinelibrary.wiley.com/doi/10.1002/fce.20230005 by Forschungszentrum Jülich GmbH Research Center, Wiley Online Library on [05/01/2024]. See the Terms and Conditions (https://onlinelibrary.wiley.com/terms-and-conditions) on Wiley Online Library for rules of use; OA articles are governed by the applicable Creative Commons License

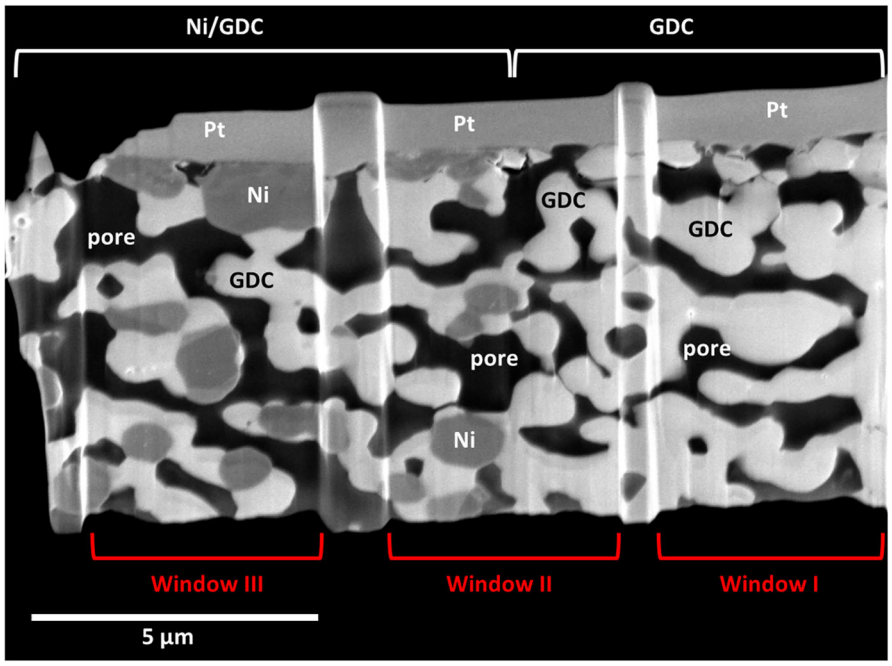

FIGURE 9 BSE (3 kV) images presenting prepared sample for transmission electron microscope (TEM) analysis from cell 3. Pt was sputtered on for preparation. Three investigated areas, window I, II and III, were thinned to about 100 nm in the Helios 4G. Three Phases are indicated. Bright phase corresponds to gadolinia doped ceria (GDC), dark grey to Ni and black to pore.

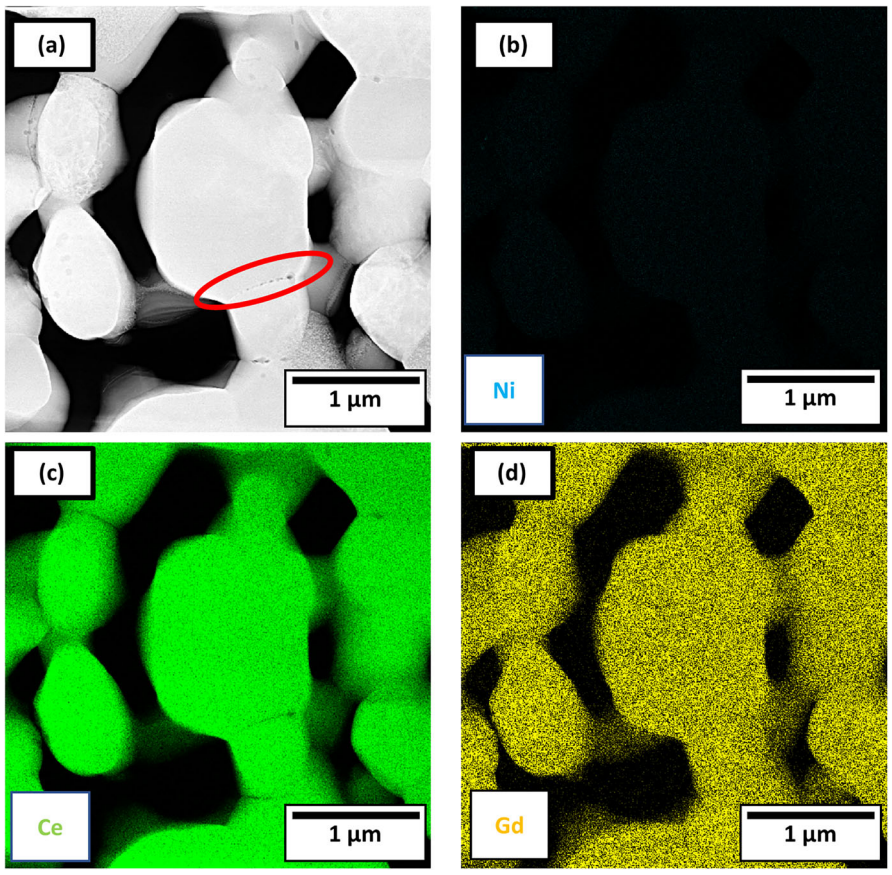

FIGURE 10 Scanning transmission electron microscopy (STEM)-EDS (200 kV high-angle annular dark-field [HAADF]) results in window I. (a) STEM image. No contrast between gadolinia doped ceria (GDC) and Ni phase because of similar average atomic mass of CeO_2 and Ni. (b) Ni distribution in blue. (c) Ce distribution in green. (d) Gd distribution in yellow.

16156854, 2023, 6, Downloaded from https://onlinelibrary.wiley.com/doi/10.1002/fuce.202300057 by Forschungszentrum Jülich GmbH Research Center, Wiley Online Library on [05/01/2024]. See the Terms and Conditions (https://onlinelibrary.wiley.com/terms-and-conditions) on Wiley Online Library for rules of use; OA articles are governed by the applicable Creative Commons License

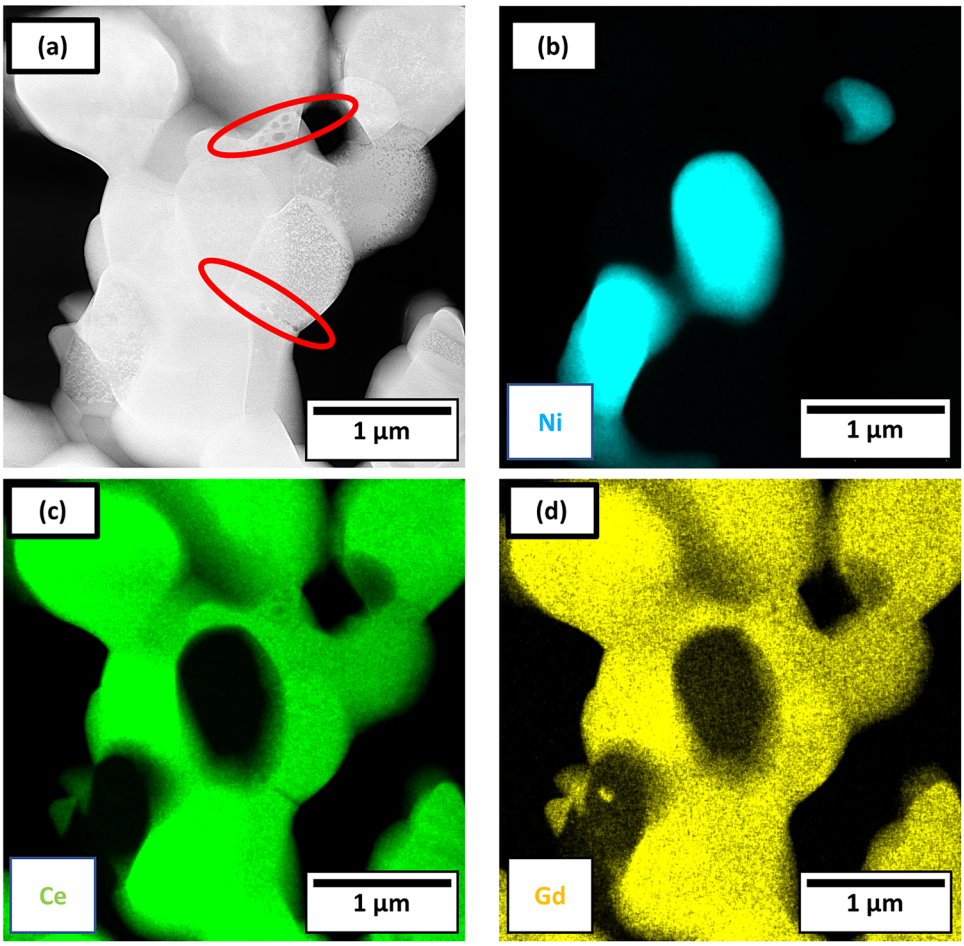

FIGURE 11 Scanning transmission electron microscopy (STEM)-EDS (200 kV high-angle annular dark-field [HAADF]) results in window II. (a) STEM image. No contrast between gadolinia doped ceria (GDC) and Ni phase because of similar average atomic mass of CeO_2 and Ni. (b) Ni distribution in blue. (c) Ce distribution in green. (d) Gd distribution in yellow.

nanopores between single GDC grains (marked area). EDS mapping of Ni, Ce and Gd, conducted with an OSIRIS ChemiSTEM microscope are given in Figure 10b–d, respectively. The mapping of Ce in Figure 10c and Gd in Figure 10d indicates that all material in this area is GDC. No sign of Ni was found in window I (Figure 10b). However, Ni on GDC-surface cannot be excluded since the sample was cut to a 100-nm thin strip and Ni on the GDC-surfaces is either below the detection limit or removed by the Ga-beam.

In the overlapping zone (window II), (Figure 11a), similar pores were found. Based on element mapping of Ni, Ce and Gd (Figure 11b–d), the identification of Ni and GDC particle in STEM image in Figure 11a is possible. No pores between Ni and GDC grains were found. The findings are similar for Figure 12, displaying the mapping of window III. The influence of nanopores between GDC particles on the performance is hard to estimate. Since they are small in number, they would not lead to a significant increase in GDC surface area.

The minor microstructural changes revealed so far might not have caused the observed increase in performance of the Ni/GDC electrode. Most likely an activation of the GDC-surfaces in the porous GDC-interlayer by interdiffused Ni is the reason for the observed improvement. Further investigations of the GDC-surfaces in the porous interlayer are necessary.

4 | CONCLUSIONS

In the present study, originally targeting accelerated degradation of a Ni/GDC fuel electrode by increased operating temperatures, an unexpected decrease in polarization resistance was observed. Operating the cell at 900°C resulted in a continuous decrease in polarization resistance over approximately one month. Considering the nominal operating temperature of 600°C, the polarization resistance decreased by about 32%. Impedance spectroscopy and subsequent DRT analysis revealed an

16156854, 2023, 6, Downloaded from https://onlinelibrary.wiley.com/doi/10.1002/fuce.202300057 by Forschungszentrum Jülich GmbH Research Center, Wiley Online Library on [05/01/2024]. See the Terms and Conditions (https://onlinelibrary.wiley.com/terms-and-conditions) on Wiley Online Library for rules of use; OA articles are governed by the applicable Creative Commons License

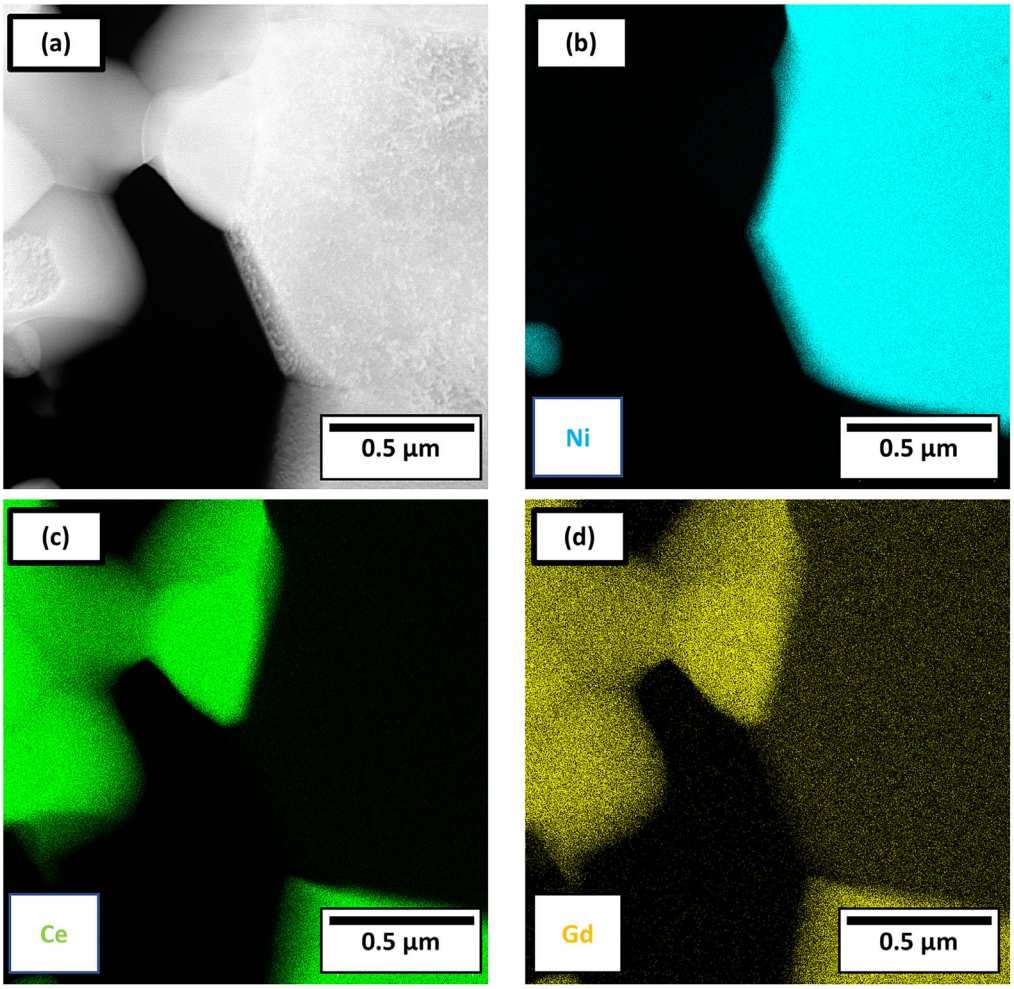

FIGURE 12 Scanning transmission electron microscopy (STEM)-EDS (200 kV HAADF) results in window III. (a) STEM image. No contrast between gadolinia doped ceria (GDC) and Ni phase because of similar average atomic mass of CeO_2 and Ni. (b) Ni distribution in blue. (c) Ce distribution in green. (d) Gd distribution in yellow.

improved charge transfer due to an increase in active reaction sites. Post-test analysis by means of SEM, EDS and FIB-SEM tomography did not show any significant microstructural or compositional changes on the µm-scale that could explain the electrode improvement. TEM analysis indicated the existence of nanopores between GDC particles but its impact on the GDC-surface area is expected to be rather small. Further nano-scale changes in GDC phase were not observed but cannot be excluded. The extension of the electrochemical active electrode into the porous GDC-interlayer is a possible explanation for the observed improvement. Ni-species deposition on the GDC-surfaces of the porous GDC-interlayer might have activated this layer. Further analysis of the GDC-surfaces will be necessary to understand the performance improvement. The results so far show that the chosen value of elevated stressor in this work might be inappropriate for accelerated stress tests for the investigated system. The applied stressor might have influenced two mechanisms with opposite effect, resulting in improvement of electrode performance.

ACKNOWLEDGMENTS

The authors gratefully acknowledge funding from the "WirLebenSOFC" Project and from the Federal Ministry of Education and Research (grant number: BMBF 03SF0622E).

Open access funding enabled and organized by Projekt DEAL.

ORCID

Yanting Liu https://orcid.org/0000-0001-5333-8927
André Weber https://orcid.org/0000-0003-1744-3732

REFERENCES

1. A. Hauch, S. D. Ebbesen, S. H. Jensen, M. Mogensen, *J. Electrochem. Soc.* **2008**, *155*, B1184.

16156854, 2023, 6, Downloaded from https://onlinelibrary.wiley.com/doi/10.1002/fuce.202300057 by Forschungszentrum Jülich GmbH Research Center, Wiley Online Library on [05/01/2024]. See the Terms and Conditions (https://onlinelibrary.wiley.com/terms-and-conditions) on Wiley Online Library for rules of use; OA articles are governed by the applicable Creative Commons License

2. F. Tietz, D. Sebold, A. Brisse, J. Schefold, *J. Power Sources* **2013**, *223*, 129.
3. A. Ringuedé, D. P. Fagg, J. R. Frade, *J. Eur. Ceram. Soc.* **2004**, *24*, 1355.
4. L. Holzer, B. Iwanschitz, T. Hocker, B. Münch, M. Prestat, D. Wiedenmann, U. Vogt, P. Holtappels, J. Sfeir, A. Mai, T. Graule, *J. Power Sources* **2011**, *196*, 1279.
5. M. Hubert, J. Laurencin, P. Cloetens, B. Morel, D. Montinaro, F. Lefebvre-Joud, *J. Power Sources* **2018**, *397*, 240.
6. S. Zha, Z. Cheng, M. Liu, *J. Electrochem. Soc.* **2007**, *154*, B201.
7. Z. Cheng, S. Zha, M. Liu, *J. Power Sources* **2007**, *172*, 688.
8. M. D. Gross, J. M. Vohs, R. J. Gorte, *J. Mater. Chem.* **2007**, *17*, 3071.
9. J. Mermelstein, M. Millan-Agorio, N. P. Brandon, *ECS Trans.* **2009**, *17*, 111.
10. A. Faes, A. Hessler-Wyser, D. Presvytes, C. G. Vayenas, J. Van Herle, *Fuel Cells* **2009**, *9*, 841.
11. B. Iwanschitz, L. Holzer, A. Mai, M. Schütze, *Solid State Ionics* **2012**, *69*, 211.
12. K. T. S. Thydén, *Ph.D Thesis*, Technical University of Denmark (Copenhagen, Denmark) **2008**.
13. Y. H. Lee, H. Muroyama, T. Matsui, K. Eguchi, *J. Power Sources* **2014**, *262*, 451.
14. A. Hagen, R. Barfod, P. V. Hendriksen, Y. L. Liu, S. Ramousse, *J. Electrochem. Soc.* **2006**, *153*, A1165.
15. A. Zekri, M. Knipper, J. Parisi, T. Plaggenborg, *Phys. Chem. Chem. Phys.* **2017**, *19*, 13767.
16. A. Nenning, C. Bischof, J. Fleig, M. Bram, A. K. Opitz, *Energies* **2020**, *13*, 987.
17. L. Blum, Q. Fang, S. M. Groß-Barsnick, L. B. de Haart, J. Malzbender, N. H. Menzler, *Int. J. Hydrogen Energy* **2020**, *45*, 8955.
18. A. Ploner, A. Hagen, A. Hauch, *Fuel Cells* **2017**, *17*, 498.
19. A. Ploner, A. Hagen, A. Hauch, *J. Power Sources* **2018**, *395*, 379.
20. M. Z. Khan, M. T. Mehran, R. H. Song, J. W. Lee, S. B. Lee, T. H. Lim, *J. Power Sources* **2018**, *391*, 94.
21. M. J. Heneka, E. Ivers-Tiffée, *ECS Trans.* **2006**, *1*, 377.
22. A. Weber, J. Szász, S. Dierickx, C. Endler-Schuck, E. Ivers-Tiffée, *ECS Trans.* **2015**, *68*, 1953.
23. C. Endler-Schuck, J. Joos, C. Niedrig, A. Weber, E. Ivers-Tiffée, *Solid State Ionics* **2015**, *269*, 67.
24. M. Trini, A. Hauch, S. De Angelis, X. Tong, P. V. Hendriksen, M. Chen, *J. Power Sources* **2020**, *450*, 227599.
25. A. Nakajo, A. P. Cocco, M. B. Degostin, P. Burdet, A. A. Peracchio, B. N. Cassenti, M. Cantoni, J. Van herle, W. K. S. Chiu, *ECS Trans.* **2017**, *78*, 3205.
26. Z. Ouyang, Y. Komatsu, A. Sciazko, J. Onishi, K. Nishimura, N. Shikazono, *J. Power Sources* **2022**, *529*, 231228.
27. Y. Komatsu, A. Sciazko, Y. Suzuki, Z. Ouyang, Z. Jiao, N. Shikazono, *J. Power Sources* **2021**, *516*, 230670.
28. N. H. Menzler, J. Malzbender, P. Schoderböck, R. Kauert, H. P. Buchkremer, *Fuel Cells* **2014**, *14*, 96.
29. D. Klotz, A. Weber, E. Ivers-Tiffée, *Electrochim. Acta* **2017**, *227*, 110.
30. W. Shi, Z. Lyu, M. Han, *ECS Trans.* **2019**, *91*, 791.
31. J. Joos, M. Ender, T. Carraro, A. Weber, E. Ivers-Tiffée, *Electrochim. Acta* **2012**, *82*, 268.
32. J. Joos, *Ph.D. Thesis*, Karlsruher Institut für Technologie (KIT) (Karlsruhe, Germany) **2015**.
33. R. M. Langford, A. K. Petford-Long, *J. Vac. Sci. Technol., A* **2001**, *19*, 2186.
34. M. Schaffer, B. Schaffer, Q. Ramasse, *Ultramicroscopy* **2012**, *114*, 62.
35. A. Müller, A. Weber, H. J. Beie, A. Krügel, D. Gerthsen, E. Ivers-Tiffée, *Proc. of the 3rd Eur. Solid Fuel Cell Forum*, Nantes, France, **1998**, 353.
36. C. Grosselindemann, N. Russner, S. Dierickx, F. Wankmüller, A. Weber, *J. Electrochem. Soc.* **2021**, *168*, 124506.
37. A. Sciazko, Y. Komatsu, T. Shimura, N. Shikazono, *J. Power Sources* **2020**, *478*, 228710.

How to cite this article: Y. Liu, F. Wankmüller, T. P. Lehnert, M. Juckel, N. H. Menzler, A. Weber, *Fuel Cells* **2023**, *23,* 430.
https://doi.org/10.1002/fuce.202300057

16156854, 2023, 6, Downloaded from https://onlinelibrary.wiley.com/doi/10.1002/fuce.202300057 by Forschungszentrum Jülich GmbH Research Center, Wiley Online Library on [05/01/2024]. See the Terms and Conditions (https://onlinelibrary.wiley.com/terms-and-conditions) on Wiley Online Library for rules of use; OA articles are governed by the applicable Creative Commons License